Growth and microstructural analysis of nanosized Y$_2$O$_3$ doped with rare-earths

Brigida Allieri [a,*], Laura E. Depero [a], Alessandra Marino [a], Luigi Sangaletti [b], Lucia Caporaso [c], Adolfo Speghini [c], Marco Bettinelli [c]

[a] *Istituto Nazionale per la Fisica della Materia and Laboratorio di Strutturistica Chimica, Università di Brescia, Via Branze 38, 25123 Brescia, Italy*
[b] *Istituto Nazionale per la Fisica della Materia and Dipartimento di Matematica e Fisica,*
Università Cattolica del Sacro Cuore, via Trieste 17-25121 Brescia, Italy
[c] *Dipartimento Scientifico e Tecnologico, Università di Verona, Strada Le Grazie, 37134 Verona, Italy*

Abstract

Nanosized cubic Y$_2$O$_3$ samples, undoped and doped with 10 mol% Nd$_2$O$_3$, Eu$_2$O$_3$, Gd$_2$O$_3$, Tb$_2$O$_3$, Ho$_2$O$_3$ and Er$_2$O$_3$ (Y$_{1.8}$Ln$_{0.2}$O$_3$, where Ln=Nd, Eu, Gd, Tb, Ho or Er), were prepared by means of a controlled hydrolysis method in an aqueous solution containing ammonia, Y(NO$_3$)$_3$ and Ln(NO$_3$)$_3$ as precursors, and a surface modifier. The microstrain and the average size of the diffraction domains have been calculated from the XRD patterns and the results have been compared with those obtained by a combustion synthesis. It is shown that the cell parameter of the C-M$_2$O$_3$ (bcc structure related to the CaF$_2$ structure; the M atom is 6-coordinated) structure of doped Y$_2$O$_3$ is correlated to the ion size of the dopant. The shape of the crystallites appears to be needle-like in all cases, while the microstrains depend on the dopant and are probably due to surface effect. XRD and Raman analysis show that, despite the heavy doping, only one phase in the Y$_2$O$_3$ powders is present. © 2000 Elsevier Science S.A. All rights reserved.

Keywords: Nanopowders; XRD; Raman; Rare-earths

1. Introduction

The development of new types of high resolution and high efficiency planar displays has created a need for optical phosphors with new or enhanced properties [1]. High efficiency phosphor materials with crystalline monodispersive fine particles are the key for the development of these new devices [2,3].

Nanophase and nanocrystalline materials, typically defined as polycrystalline solids with particle diameter of less than 100 nm, offer new possibilities for advanced phosphor applications. In fact, the bulk properties of those materials depend on the high percentage of grain boundaries, although the local atomic structure at the interfaces is not completely understood [4–6]. In particular, lanthanide ions in insulating hosts find uses in a variety of applications such as phosphors for fluorescent lighting, display monitors, X-rays imaging, scintillators and amplifiers for fiber-optics communication [7–9]. Besides their intrinsic interest, nanocrystalline materials also provide model systems for studying the effect of surfaces on bulk properties.

The luminescence efficiency of these materials is often limited by the dynamics of the lanthanide ion, which depends on the interactions with the insulating host and therefore the lanthanide dopant can be used as a sensitive probe of the chemistry and structure of its host. Moreover, it has been shown that the quantum efficiency of the luminescence of doped nanocrystals increases as the size of the crystals decreases [10,11]. Another advantage of nanosized materials is that the presence of the impurity transfers the dominant recombination route from the surface of the nanocrystals to the dopant states, so that passivation of the surface is not crucial.

In a recent communication, preliminary results have been reported on the synthesis, characterization and optical spectroscopy of nanosized doped Y$_2$O$_3$ prepared by a combustion method [12], a well-known oxide phosphor material which shows improved quantum efficiency when prepared in a nanostructured form. Moreover, the mixed rare earth-yttrium oxides (Re$_x$Y$_{2-x}$O$_3$) are a novel group of diluted magnetic semiconductors [13]. In recent studies it was shown that the distribution of the magnetic ions in the C-M$_2$O$_3$ (bcc structure related to the CaF$_2$ structure; the M atom is 6-coordinated) affects the magnetic properties of these materials [14,15].

* Corresponding author. Tel.: +39-030-3715406; fax: +39-030-3702448.
E-mail address: allieri@tflab.ing.unibs.it (B. Allieri).

The aim of this paper is the study of microstructure properties (strain and average size of the diffraction domains) of the lanthanide-doped cubic phase Y_2O_3 depending on the doping. In particular, we describe the synthesis by wet route and the structural analysis of nanocrystalline cubic Y_2O_3 doped with Nd, Eu, Gd, Tb, Ho, and Er ions, comparing the results obtained with the same set of samples synthesized by a combustion method [16]. The structural characterization of the samples has allowed to state that, in spite of the heavy doping, a monophasic Y_2O_3 powder has been obtained and that the rare earth ions substitute Y in the lattice of the oxide. The results obtained in this paper confirmed our previous results [16] and are in agreement with those reported in the paper by Mitric et al. [17] in which the crystal size and the microstrain of Y_2O_3 powder doped with Sm at different concentrations were evaluated.

2. Experimental

Nanosized cubic Y_2O_3 samples, undoped and doped with 10 mol% Nd_2O_3, Eu_2O_3, Gd_2O_3, Tb_2O_3, Ho_2O_3 or Er_2O_3 ($Y_{1.8}Ln_{0.2}O_3$, where Ln=Nd, Eu, Gd, Tb, Ho or Er), were prepared by using a wet synthesis procedure reacting an alcoholic solution containing $Y(NO_3)_3$ and $Ln(NO_3)_3$ with a basic solution of a surface modifier at pH>10 [18]. The two solutions were mixed and the obtained gel was centrifuged for 1 h at 3000 rpm of speed. After removing the aqueous solution the powder was dried in a stove at 70°C for 24 h and then heat treated at 500°C for 12 h.

Structural characterization of all samples has been made by using X-rays diffraction, microraman spectroscopy and scanning electron microscopy. The diffraction experiments were performed on a Philips MPD 1830 automated powder
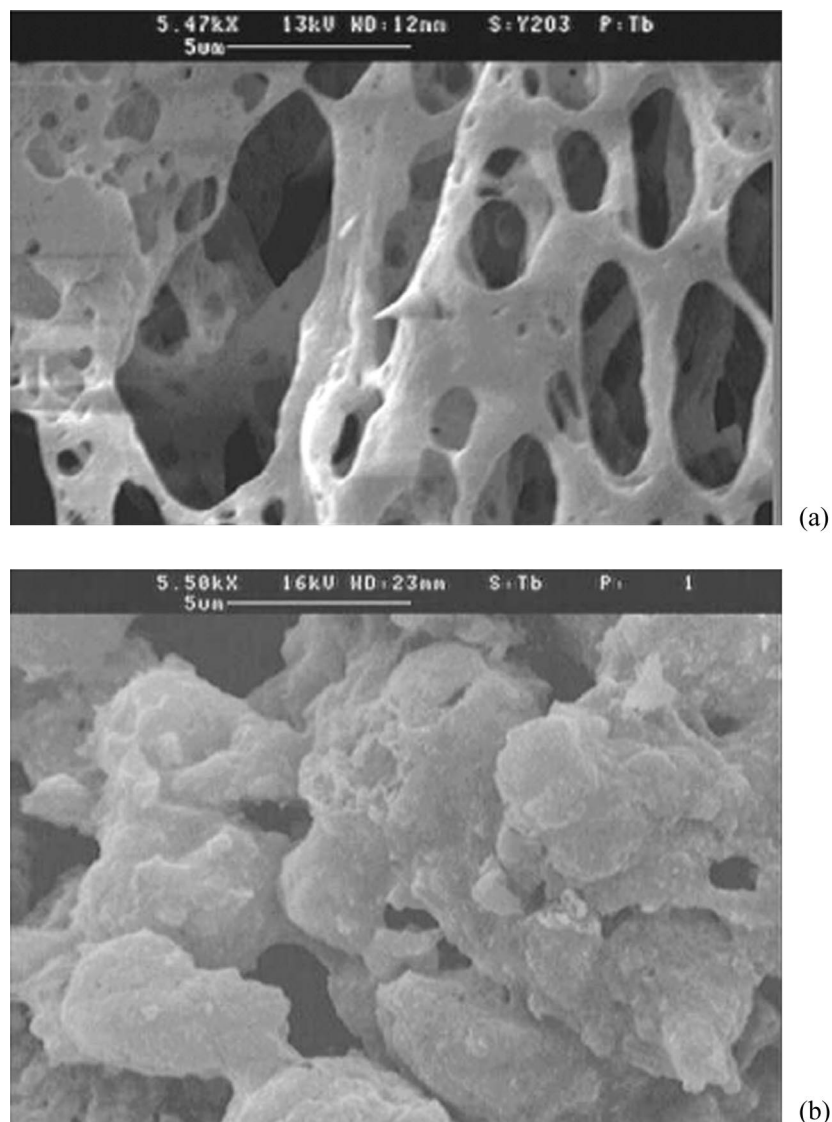

(a)

(b)

Fig. 1. SEM micrographs of the Y_2O_3 samples doped with Tb and prepared by combustion (a) and wet synthesis (b).
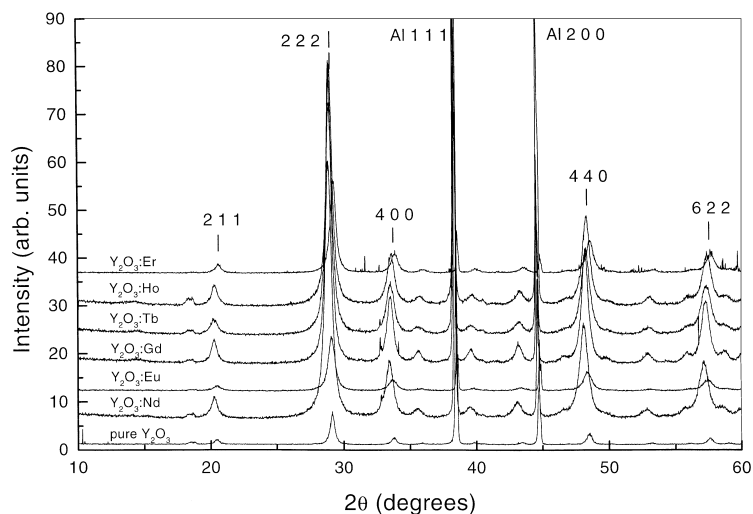
Fig. 2. XRD patterns of the pure and rare earths doped samples. The reflections used for the profile analysis are indicated together with two peaks of the aluminum powders added to the sample as internal 2θ reference.

diffractometer with graphite-monochromated Cu Kα radiation in the Bragg–Brentano parafocusing geometry. Diffraction patterns have been collected for pure and rare earths doped (about 10%) Y_2O_3 nanopowders. Aluminum powder has been added to the samples as internal 2θ reference. The profile of the diffraction peaks were Fourier analyzed by means of a program developed by Lutterotti and Scardi [19] and based on algorithms derived by Nandi et al. [20]. The instrumental function, to be deconvoluted from the observed profile, was determined by measuring the diffraction pattern of a standard KCl powder and the microstructural parameters $\langle M \rangle$ (average size of the diffraction domains) and $\langle \varepsilon^2 \rangle^{1/2}$ (mean-square root microstrain) were evaluated. Moreover, the structural parameter a of the Y_2O_3 cubic cell was calculated by using the NDSU (Least Square Unit Cell Refinement) program, version 86.2.

Microraman measurements were carried out with a Dilor Labram spectrograph equipped with $1800 \, \mathrm{l \, mm^{-1}}$ gratings and a CCD detector cooled at about $230 \, \mathrm{K}$. The microscope was confocally coupled to the spectrograph. A He-Ne laser with a power at the sample of less than $10 \, \mathrm{mW}$ was used as exciting source ($\lambda = 632.8 \, \mathrm{nm}$).

SEM images have been collected with a Cambridge Stereoscan 260 Microscope equipped with a Link Analytical probe for Energy Dispersion X-ray Spectroscopy (EDXS) analysis.

3. Results and discussion

EDXS analysis confirms the yttrium/rare earth ratio (10 mol%) and the homogeneity of the samples. As shown in Fig. 1, the two methods of synthesis determine a very different morphology of the powders. In particular for all the samples made by the combustion route a spongy-like

structure is clearly seen, while the wet synthesized samples appear to be powdery.

In Fig. 2, the diffraction patterns of the pure and rare earth doped samples are shown and the most intense reflections of the Y_2O_3 are indicated (C-M_2O_3 structure [21]). The cell parameter of the Y_2O_3 cubic cell, calculated by considering five reflections, increases with the ionic radius of the dopant almost following a linear behavior (Table 1 and Fig. 3). We obtained comparable results analyzing the same set of samples synthesized by a combustion method [16]. These results show that the trend of the cell parameter mainly depends on the doping and it is not a function of the synthesis route, while for the same dopant, the synthesis strongly influences the microstrain.

The cell parameters calculated for the doped samples made by both synthesis routes have been fitted against the ionic radius of the dopant [22] by linear function and the errors on the parameters has been evaluated (Fig. 3). For a given dopant, the powders made by the wet synthesis show a larger cell parameter than that of the samples made by combustion, while the average size of crystallites is smaller. The higher χ^2 factor obtained in the linear fitting of the wet samples set may be due to a difficulty in controlling this synthesis.

Table 1

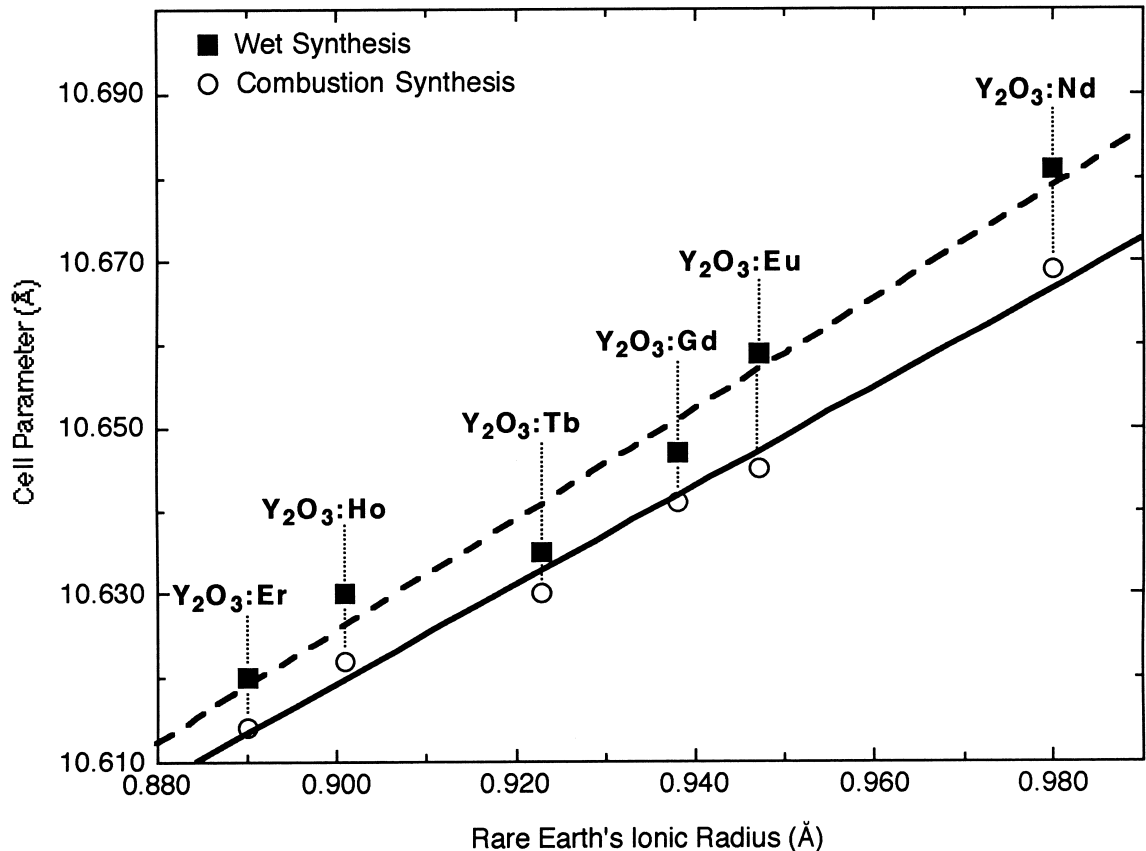| Sample	Cell parameter (Å)	Raman shift (cm^{-1})	Rare earth ionic radius (Å) [22]
Y_2O_3:Nd	10.681 ± 0.0025	370	0.980
Y_2O_3:Eu	10.659 ± 0.0022	371	0.947
Y_2O_3:Gd	10.647 ± 0.0030	374	0.938
Y_2O_3:Tb	10.635 ± 0.0036	373	0.923
Y_2O_3:Ho	10.630 ± 0.0044	–	0.901
Y_2O_3:Er	10.620 ± 0.0008	–	0.890
Pure Y_2O_3	10.616 ± 0.0033	377	

Fig. 3. Calculated cell parameter of doped Y_2O_3 samples synthesized by wet and combustion methods as a function of the ionic radius of the rare earth. The data have been fitted by a linear function.

In Fig. 4, the average size ($\langle M \rangle$) of the diffraction domains of all samples are plotted in polar coordinates as a function of the angles between the [1 0 0] directions, taken as reference, and the [1 1 1], [3 1 1], and [2 1 1] directions (Fig. 2). The average sizes are in agreement with those obtained by Mitric et al. [17] in which Y_2O_3 powder samples doped with Sm at different concentrations were studied.

The angles between the planes have been calculated by using the following expression:

$$\cos \phi = \frac{\boldsymbol{r}^*_{H1} \boldsymbol{r}^*_{H2}}{r^*_{H1} r^*_{H2}}$$

where the vector of the reciprocal lattice $\boldsymbol{r}^*_{Hn} = h_n \boldsymbol{a}^* + k_n \boldsymbol{b}^* + l_n \boldsymbol{c}^*$ is normal to the family of lattice planes (hkl) [23]. In this way it is possible to have a rough idea of the shape of the crystallites. All samples show a needle-like shape ($\langle M \rangle$ varies in a range from 4 to 12 nm) that actually is not correlated to the morphology as seen by SEM analysis. Similar behavior has been observed in the samples synthesized by combustion method.

Furthermore, in Fig. 5 the microstrains of doped and pure Y_2O_3 synthesized by wet method are shown. The microstrain of pure Y_2O_3 is about one third than that obtained for

the doped samples. The similarity between Er and Y ionic radii may justify the low microstrain obtained in the Er and Ho doped samples. A monotonic behavior of the microstrains with the ionic radii is shown, with the exception of the Y_2O_3:Gd sample. In the hypothesis of a random distribution of the doped ions in the two non equivalent cation sites of the C-M_2O_3 structure, a larger difference in the ionic radii may induce higher microstrain in the structure. The maximum microstrains are obtained for Y_2O_3:Nd sample. It is worth to note that, differently from the other doping cation forming C-M_2O_3 structure as Y_2O_3, Nd_2O_3 at room temperature has a A-M_2O_3 (bcc structure related to the CaF_2 structure. The M atom is 7-coordinated) type of structure [20]. A striking feature of the A-M_2O_3 is the unusual 7-coordination of the metal atoms, that may be the origin of the large microstrain present in the Y_2O_3:Nd sample.

In the case of Gd doped Y_2O_3 it has been shown evidence of cation ordering in the two non equivalent sites of the structure [14], that may justify in our results the minimum in the microstrains found for the Y_2O_3:Gd sample.

In Fig. 6, the linear correlation between $\langle \varepsilon^2 \rangle^{1/2} \langle M \rangle$ and $\langle M \rangle$ calculated by considering only the reflection at $2\theta = 29°$ of all doped samples is shown. All the points corresponding to both the combustion and wet series of samples have been
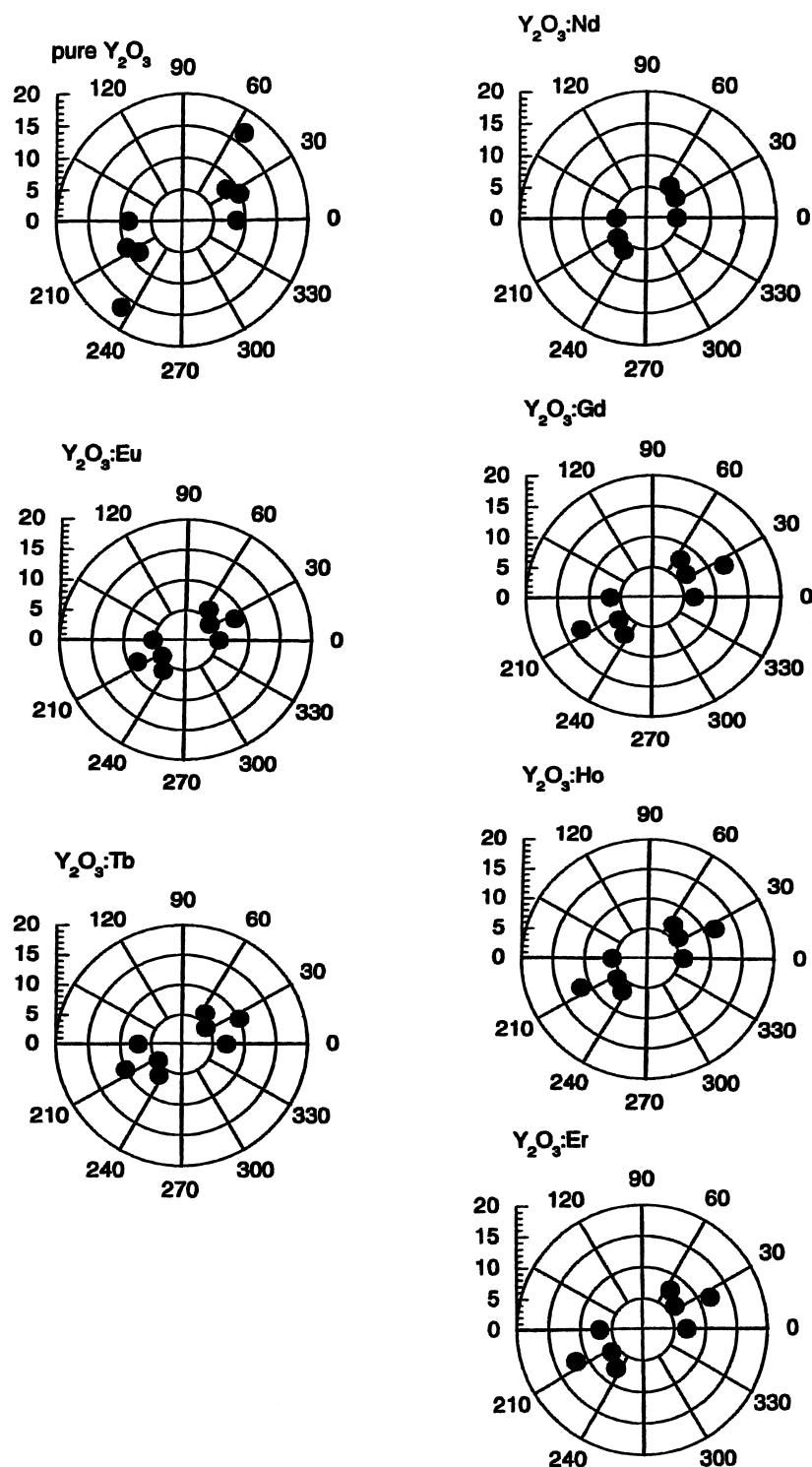
Fig. 4. Polar plot of the average size ($\langle M \rangle$) of the diffraction domains of all samples as a function of the angles between a [1 0 0] directions, taken as reference, and the [1 1 1], [3 1 1] and [2 1 1] directions.

fitted by a straight line. A similar behavior has been pointed out in a previous work for rutile and anatase phases of pure and doped TiO_2 nanopowders [24]. In that case, even though the trend is similar, only for the rutile samples the correlation is truly linear. For Y_2O_3 nanopowders as in the case of TiO_2, the constant term of the straight line is fixed to zero. The

good fitting supports the hypothesis that microstrains depend mainly on the surface, since no microstrains are expected in the case of infinite size crystallites.

Even if a good linearity is detected for the Y_2O_3 doped samples, the angular coefficient of the straight line is higher than that found for TiO_2 phases. It can be thus suggested
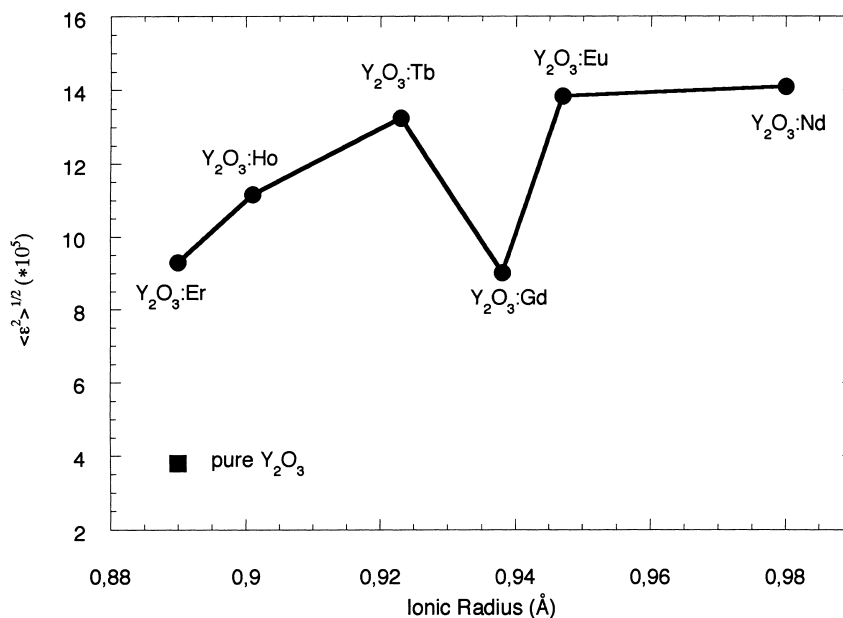
Fig. 5. Mean square root microstrains of the doped Y_2O_3 samples made by wet synthesis and calculated by using the 1 1 1 reflection ($2\theta=29°$), as a function of the ionic radius. The value of the pure Y_2O_3 is shown as reference.

that in the Y_2O_3 structure higher microstrains are induced by the surface.

Finally, the microraman spectra of the doped as well as the pure Y_2O_3 powders confirm the homogeneity of the samples. In agreement with the XRD analysis, only one phase (i.e. one single band of the Raman spectrum) is observed despite the heavy doping of the Y_2O_3 matrix.

In Fig. 7, a shift of the Y_2O_3 signal towards smaller wavenumbers as the ionic radius and the mass of the dopant increases (Table 1) can be seen. This may be explained by considering that the wavenumber is inversely proportional to the square root of the mass, while the elastic constant is negligibly influenced by the substitution of yttrium. Indeed, in this set of samples the value of the Raman shift of the
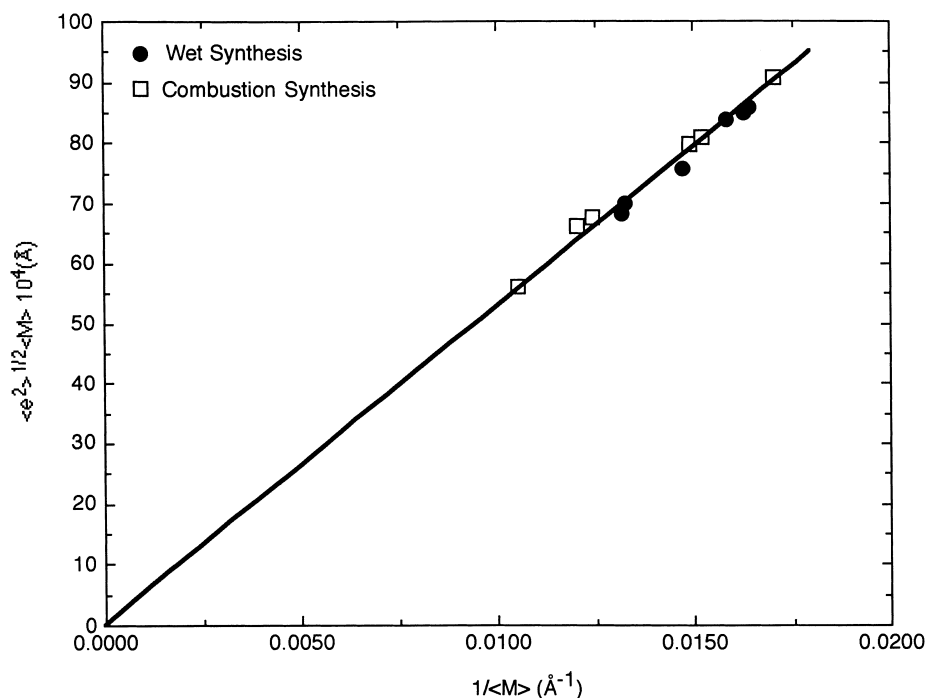

Fig. 6. $\langle\varepsilon^2\rangle^{1/2}\langle M\rangle$ as a function of $\langle M\rangle$. The values refer to a 1 1 1 reflection ($2\theta=29°$) and have been fitted by a straight line shown in the figure.
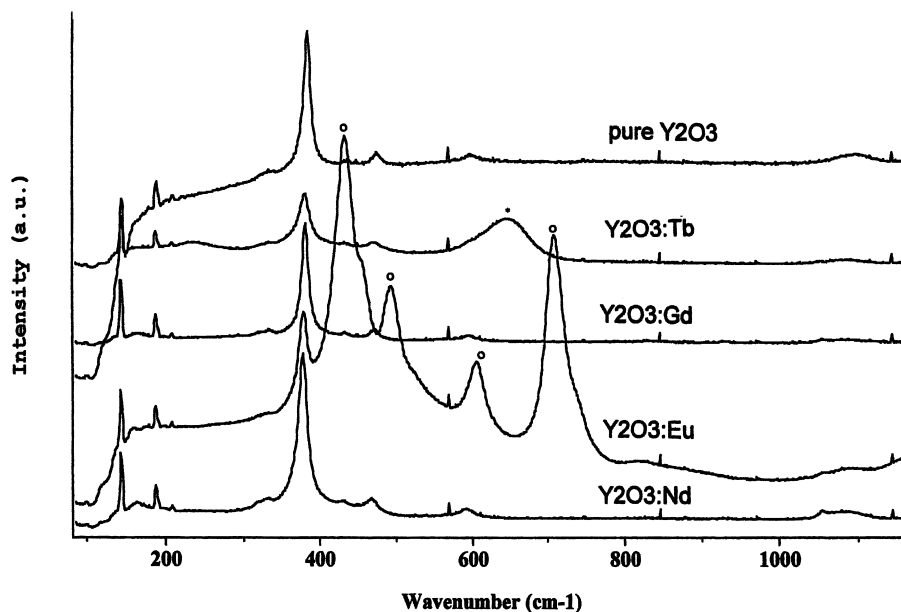
Fig. 7. Raman shift of pure and Nd, Eu, Gd and Tb doped Y_2O_3 nanopowders. The Raman shift for Ho and Er doped Y_2O_3 samples could not be determined because of the strong luminescence present in the same spectral region. The labels o and * indicate the contribution of the Eu and Tb luminescence, respectively.

one doped with Tb is unexpectedly high; by the way, a shift of this signal may be due to the high background.

4. Conclusions

In this work the microstructure properties of the lanthanide-doped Y_2O_3 nanopowders obtained by wet synthesis are discussed.

The main conclusions are the following.

- There is no correlation between the morphology of the samples and the needle-like shape of the crystallites as determined by profile analysis of the diffraction patterns.
- The cell parameters of the C-Me_2O_3 structure of Ln:Y_2O_3 samples are linearly correlated with the ionic radii of the dopant. The relatively large dispersion of the cell parameters of the sample made by the wet method may be due to a difficulty in controlling this synthesis.
- The wet synthesis produces smaller crystallites with respect to the combustion one. This fact may be correlated to the larger cell parameters obtained for the same doping in the former case.
- The microstrain of the pure Y_2O_3 is about one third of those obtained for the doped samples. The correlation between the microstrain and the ionic radii may depend on the difference with the dimension of the Y ion (close to that of the Er ion). The exception of the Gd:Y_2O_3 sample may be ascribed to an ordering in one of the two non-equivalent cation sites of the C-Me_2O_3 structure.
- The analysis of the correlation between $\langle \varepsilon^2 \rangle^{1/2} \langle M \rangle$ and $\langle M \rangle$ indicates that the microstrains are mainly due to surface constrains.

- A consistent shift of the Y_2O_3 Raman signal with the mass of the dopant is shown, confirming that in all samples the Ln substitutes the Y ion in the Y_2O_3 structure.

References

[1] P. Maestro, D. Huguenin, J. Alloys Comp. 225 (1995) 520.
[2] R.P. Rao, J. Electrochem. Soc. 143 (1996) 189.
[3] S. Erdie, R. Roy, et al., Mater Res. Bull. 31 (1996) 1013
[4] R.W. Siegel, G.J. Thomas, Ultramicroscopy 40 (1992) 376.
[5] R.W. Siegel, J. Phys. Chem. Solids 55 (1994) 1097.
[6] R.W. Siegel, in: D. Wolf (Ed.), Materials Interfaces: Atomic-Level Structure and Properties, Chapman & Hall, London, 1992, p. 431.
[7] C. Fouassier, Curr. Opin. Solid State Mater. Sci. 2 (1997) 231.
[8] G. Blasse, J. Alloys Comp. 225 (1995) 529.
[9] G. Blasse, B.C. Grabmaier, Luminescent Materials, Springer, Berlin, 1994.
[10] E.T. Goldburt, B. Kulkarni, R. Bhargava, J. Taylor, M. Libera, J. Lumin. 190 (1997) 72–74.
[11] T. Ye, Z. Guiwen, Z. Weiping, X. Shangda, Mater. Res. Bull. 32 (1997) 501.
[12] G. Tessari, M. Bettinelli, A. Speghini, D. Ajò, G. Pozza, L.E. Depero, B. Allieri, L. Sangaletti, Appl. Surf. Sci. 144/145 (1999) 686–689.
[13] M. Mitric, P. Onnerud, D. Rodic, R. Tellgren, A. Szytula, M.Lj. Napijalo, J. Phys. Chem. Solids 54 (1993) 967.
[14] D. Rodic, B. Antic, M. Mitric, J. Magnetism Magn. Mater. 140–144 (1995) 1181–1182.
[15] B. Antic, M. Mitric, D. Rodic, J. Magnetism Magn. Mater. 145 (1995) 349–356.
[16] B. Allieri, et al., unpublished results.
[17] M. Mitric, A. Kremenovic, R. Dimitrijevic, D. Rodic, Solid State Ionics 101–103 (1997) 495–501.
[18] P.K. Sharma, R. Nass, H. Schmidt, Opt. Mater. 10 (1998) 161.

[19] L. Luterotti, P. Scardi, General Peak Separation Routine — MARQ-FIT (1990) and Line Broadening Analysis by W.A.X.S. (1992).

[20] R.K. Nandi, H.K. Kuo, W. Shosberg, G. Wissler, J.B. Cohen, B. Crist Jr., J. Appl. Cryst. 17 (1984) 22.

[21] Structural Inorganic Chemistry, A.F. Wells (Ed.), Oxford Science Publications, Oxford, p. 545C.

[22] Y.Q. Jia, Crystal radii and effective ionic radii of the rare earth ions, J. Solid State Chem. (1991) 184–186.

[23] C. Giacovazzo, et al. (Eds.), Fundamentals of Crystallography, Oxford Science Publications, Oxford, p. 125.

[24] L.E. Depero, L. Sangaletti, B. Allieri, E. Bontempi, A. Marino, M. Zocchi, J. Crystal Growth 198/199 (1999) 516–520.